Zhang X, Lu S, Wang SH *et al.* Diagnosis of COVID-19 pneumonia via a novel deep learning architecture. JOURNAL OF COMPUTER SCIENCE AND TECHNOLOGY 37(2): 330–343 Mar. 2022. DOI 10.1007/s11390-020-0679-8

Diagnosis of COVID-19 Pneumonia via a Novel Deep Learning Architecture

Xin Zhang[1,♯] (张 鑫), Siyuan Lu[2,♯] (陆思源), Shui-Hua Wang[3,4,♯] (王水花), Xiang Yu[2,♯] (余 翔)
Su-Jing Wang[5,6] (王甦菁), Lun Yao[7] (姚 仑), Yi Pan[8] (潘 毅), and Yu-Dong Zhang[2,9,*] (张煜东)

[1] *Department of Medical Imaging, The Fourth People's Hospital of Huai'an, Huai'an 223002, China*

[2] *School of Informatics, University of Leicester, Leicester, LE1 7RH, U.K.*

[3] *School of Architecture Building and Civil Engineering, Loughborough University, Loughborough, LE11 3TU, U.K.*

[4] *School of Mathematics and Actuarial Science, University of Leicester, Leicester, LE1 7RH, U.K.*

[5] *Key Laboratory of Behavior Sciences, Institute of Psychology, Chinese Academy of Sciences, Beijing 100101, China*

[6] *Department of Psychology, University of the Chinese Academy of Sciences, Beijing 100101, China*

[7] *Department of Infection Diseases, The Fourth People's Hospital of Huai'an, Huai'an 223002, China*

[8] *Department of Computer Science, Georgia State University, Atlanta 30302-5060, U.S.A.*

[9] *Department of Information Systems, Faculty of Computing and Information Technology, King Abdulaziz University Jeddah 21589, Saudi Arabia*

E-mail: hasyzx@njmu.edu.cn; siyuan_lu@foxmail.com; shuihuawang@ieee.org; xy144@le.ac.uk
wangsujing@psych.ac.cn; jshayl@163.com; yipan@gsu.edu; yudongzhang@ieee.org

Received June 3, 2020; accepted March 30, 2021.

Abstract COVID-19 is a contagious infection that has severe effects on the global economy and our daily life. Accurate diagnosis of COVID-19 is of importance for consultants, patients, and radiologists. In this study, we use the deep learning network AlexNet as the backbone, and enhance it with the following two aspects: 1) adding batch normalization to help accelerate the training, reducing the internal covariance shift; 2) replacing the fully connected layer in AlexNet with three classifiers: SNN, ELM, and RVFL. Therefore, we have three novel models from the deep COVID network (DC-Net) framework, which are named DC-Net-S, DC-Net-E, and DC-Net-R, respectively. After comparison, we find the proposed DC-Net-R achieves an average accuracy of 90.91% on a private dataset (available upon email request) comprising of 296 images while the specificity reaches 96.13%, and has the best performance among all three proposed classifiers. In addition, we show that our DC-Net-R also performs much better than other existing algorithms in the literature.

Keywords pneumonia, COVID-19, convolutional neural network, AlexNet, deep learning

1 Introduction

Since December 2019, the coronavirus disease 2019 (COVID-19) has become a worldwide public health security challenge. World Health Organization (WHO) has confirmed its pathogen and named it 2019-new coronavirus (2019-nCOV), and the International Committee on Taxonomy of Viruses (ICTV) has designated

Regular Paper

This paper was supported by the Royal Society International Exchanges Cost Share Award of UK under Grant No. RP202G0230, the Medical Research Council Confidence in Concept Award of UK under Grant No. MC_PC_17171, the Hope Foundation for Cancer Research of UK under Grant No. RM60G0680, the British Heart Foundation Accelerator Award of UK under Grant No. AA/18/3/34220, Sino-UK Industrial Fund under Grant No. RP202G0289, the Global Challenges Research Fund (GCRF) of UK under Grant No. P202PF11, the Fundamental Research Funds for the Central Universities of China under Grant No. CDLS-2020-03, the Key Laboratory of Child Development and Learning Science (Southeast University), Ministry of Education of China, Henan Key Research and Development Project of China, under Grant No. 182102310629, and the National Natural Science Foundation of China under Grant Nos. U19B2032 and 61772511.

♯Xin Zhang, Siyuan Lu, Shui-Hua Wang, and Xiang Yu contributed equally to this paper

*Corresponding Author

this novel coronavirus as SARS-CoV-2. 2019-nCoV has strong adaptability; it can be more effectively transmitted from person to person and may have increased toxicity compared with influenza [1]. 2019-nCoV can be detected in human respiratory tract epithelial cells within roughly 96 hours after infection. The COVID-19 is highly contagious, spreading worldwide at an alarming rate, and the number of confirmed cases is increasing. Some patients' disease progresses rapidly, leading to severe and critical illness, and even death. The identification of COVID-19 relies on epidemiology, clinical symptoms, imaging performance, and laboratory tests.

The diagnosis of COVID-19 is proved to be effective using viral nucleic acid (NA) detection, which has robust specificity with meagre sensitivity. However, the diagnosis is greatly affected by the samplers and the sampling points. There are many false-negative cases during the viral NA test that are tested positive with computerized tomography (CT). These include cases of multiple false-negatives that are diagnosed positive through repeated sampling [2]. These findings show that CT preliminary screening is important in some cases. In addition, viral NA lacks available tests and supplies, and the feedback of the test results requires a certain amount of time. These challenges may delay the treatment and isolation of patients, increasing the infection risk of people around them.

CT is a quick and straightforward technique for screening infected patients. Some experts recommend using time-saving chest calculations to diagnose suspicious cases with CT instead of real-time polymerase chain reaction (RT-PCR), a viral NA detection method①. The CT function of early COVID-19 detection has not been specially researched, which is crucial for the early detection of suspicious cases, even in asymptomatic patients. When the NA test result shows false negatives, the CT test is especially important. It is one of the most critical approaches for the early diagnosis of pneumonia caused by the novel coronavirus. CT has a big impact on judging the nature, progression and prognosis of the lesion, evaluating the severity of the disease, and guiding clinical classification. In the face of sudden outbreaks, making full use of CT's advantages deserves discussing, thinking and investment.

In the meantime, signal processing, artificial intelligence, and deep learning (DL) technologies have successfully been applied in biomedical image analysis, computing, and modelling. Lu [3] proposed radial-basis-function neural networks (RBFNNs) for classifying pathological brains. Based on extreme learning machine (ELM), Yang [4] presented a kernel-based version (K-ELM) for creating a novel pathological brain detection system. Their method is robust and effective. Lu [5] proposed a novel extreme learning machine trained by the bat algorithm (ELM-BA) approach. Li and Liu [6] introduced the real-coded biogeography-based optimization (RCBBO) to detect diseased brains. Jiang [7] used a six-layer CNN (6L-CNN) to recognize sign language fingerspelling. Szegedy *et al.* [8] presented the GoogleNet, which achieved incredible performance on ImageNet Large-Scale Visual Recognition Challenge (ILSVRC) 2014. Yu and Wang [9] suggested the use of ResNet18 for mammogram abnormality detection.

In all, there are successful reports showing that computers can help medical image analysis. However, one common challenging task in the above systems or models is to improve the performance without introducing overcomplicated structures. To effectively select good features in high dimensional domains, a method named minimal-redundancy-maximal-relevance criterion (mRMR) is introduced in [10]. The authors [10] claimed that superior features can be selected at low cost, justified by extensive experiments on different datasets with different classifiers.

Nevertheless, a deep neural network (DNN) may suffer from overfitting, and its accuracy can still be improved using different architectures and algorithms. In this study, we use classical AlexNet as the backbone, and we propose two improvements. 1) We add batch normalization to reduce internal covariance shift and accelerate the training. 2) We replace the fully connected layer in AlexNet with three classifiers: SNN, ELM, and RVFL. Therefore, we propose three deep neural network architectures: DC-Net-SNN, DC-Net-ELM, and DC-Net-RVFL based on three different randomized neural networks, for the task of detecting COVID-19. We select the best model among DC-Net-SNN, DC-Net-ELM, and DC-Net-RVFL as the most suitable model.

The structure of our paper is as follows. Section 2 and Section 3 present the background and the dataset, respectively. Section 4 provides the rationale for our methods. Section 5 configures the experimental settings. Section 6 presents the discussions and results. Finally, Section 7 concludes the paper.

① https://enapp.chinadaily.com.cn/a/202002/06/AP5e3be074a3103a24b1106147.html, June 2020.

2 Background

The chest CT (CCT) images of patients with COVID-19 show patchy ground-glass (GG) opacity in the subpleural area of both lungs, as well as pulmonary consolidation. The typical discoveries of COVID-19 on CCT are GG opacities of bilateral pulmonary parenchyma, combined with pulmonary consolidation, and sometimes round lesions distributed around the lungs [11].

In the computer science community, Adrian Rosebrock② presented a guide for using deep learning (Keras and TensorFlow) to detect COVID-19. This guide can help readers learn sample diseased and healthy X-ray images, train CNNs to detect COVID-19 automatically, and evaluate their results. Maghdid *et al.* [12] shared a low-cost technique of using smartphone embedded sensors to diagnose COVID-19. This approach is particularly helpful since many people are currently holding smartphones every day. Wang and Wong [13] published a DL framework (COVID-Net) adapted for detecting COVID-19 patients based on chest radiography scans. They also used an explainable method to acquire more meaningful understandings into vital elements linked with COVID cases. Staff in the University of Delft developed a software package called CAD4COVID③, an AI software that triages suspected patients with COVID-19 on chest X-rays scans and indicates those affected lung tissues. More notable work can be found in [14].

Although the CT performance of detecting COVID-19 has certain characteristics, similar characteristics can also be found for pulmonary bacterial infections, fungal infections, pulmonary haemorrhage, pulmonary edema, and other viral pneumonia diseases. Therefore, it is difficult to distinguish them at diagnosis.

Judging from the current situation, the sensitivity of CT diagnosis is higher than that of NA detection. However, due to the inherent characteristics of image diagnosis, different lesions can show similar image manifestations. These characteristics will result in low specificity and inevitably overdiagnosis.

A patient can have numerous lung lesions due to different causes, causing fluctuations in rate of disease progression, which will require multiple imaging in a short time, significantly increasing the workload of the diagnostician. Therefore, the integration of AI into the diagnosis and treatment process of lung infections or other infectious diseases is worthy of further study.

Specific questions in this field include: how to provide doctors with diagnosis and treatment opinions quickly and accurately, how to alleviate the shortage of clinical radiologists, and how to increase efficiency in disease prevention and control.

From the viewpoint of computer science, most current AI methods are not comparable to radiology experts. The data, models, and codes of recently published papers in the area of AI for COVID-19 are not readily available. Therefore, we expect that our study can contribute to the community greatly. The codes, the data, and the model will be open to the public upon the acceptance of this paper④.

3 Dataset

Using a systematic random sampling method, 66 patients are randomly selected. The new coronavirus pneumonia is in the observation group: 44 males and 22 females, aged from 23 years to 91 years, with an average age of (49.48 ± 14.71) years. The control group is selected from individuals participating in routine health checkup: 38 males and 28 females, aged from 25 years to 72 years. The checkup group's average age is (38.44 ± 10.58) years. Criteria for confirmed COVID-19 include: 1) a positive NA test and 2) a complete CT image (CTI) data.

During image acquisition, CT scanning configurations are set as follows: Philips Ingenuity 64-row spiral CT machine, low kilovoltage (KV): 120, milliampere-seconds (mAs): 240, layer thickness 3 mm, layer spacing 3 mm, screw pitch 1.5: lung window (W: 1500, L: -500), Mediastinum window (W: 350, L: 60), thin layer reconstruction according to the lesion display, the layer thickness and the layer distance are 1 mm lung window image. The patients are placed in a supine position, breathing deeply after holding in, and conventionally scanned from the lung tip to the costal diaphragm angle. Each image is of size 512×512 pixels.

All images are transmitted to the medical image PACS for observation, and two radiologists with rich chest diagnostic experience collectively read the radiographs and record the distribution, size and morphology of the CT manifestations of the lesions. Up to 1–4

②https://www.pyimagesearch.com/2020/03/16/detecting-covid-19-in-x-ray-images-with-keras-tensorflow-and-deep-learning, June 2020.

③https://www.delft.care/cad4covid, July 2020.

④https://github.com/SiyuanLuLSY/Diagnosis-of-COVID-19-pneumonia-via-a-novel-deep-learning-architecture, Mar. 2022.

slices are chosen. When there are disagreements between the two analyses, a superior doctor is consulted to reach a consensus. The slice-level selection method is: for COVID-19 pneumonia patients, the selected slice showing the largest size and the number of lesions is selected. For normal subjects, any level of the image can be selected.

Fig.1 shows two example CT images of the COVID-19 dataset we used in this study. The dataset is available upon email request. In total, we collect 296 lung window images from CCT. For evaluation, we use the hold-out method. Up to 70% are used for training, and the remainder 30% are for testing. The summary of the dataset is presented in Table 1.

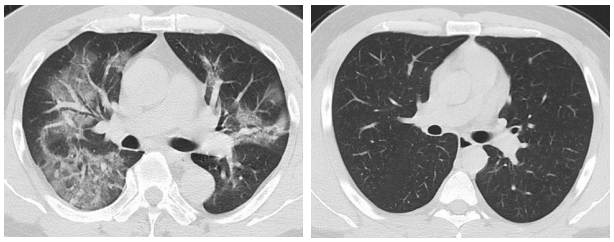

(a) (b)

Fig.1. Example images from our COVID-19 dataset. (a) COVID-19 patient. (b) Healthy. In (a), the patchy GG opacity lesions are shown in the COVID-19 patients' CITs. For CTIs from healthy people, there are no visualizable lesions.

Table 1. Number of Images in Hold-Out Setting

Set	COVID-19	Healthy
Training	104	104
Test	44	44
Total	148	148

4 DC-Net

4.1 Using AlexNetas as Backbone

AlexNet is a well-known neural network proposed by Krizhevsky *et al.* [15] for ILSVRC-2012. It has achieved significantly higher accuracy than its competitors in image classification, leading to the refocus of research interest in using DNNs as universal approximators. AlexNet is built upon the concept of multi-layered convolutional neural networks, introduced by LeNet, and fueled by the rapid increase of computational power with graphics processing units (GPUs). AlexNet has been applied in multiple fields, including biomedical analysis, object detection, etc.

The reason why we use AlexNet as the backbone is that overfitting can be avoided using AlexNet concerning our binary classification task. Also, the computational cost of AlexNet is efficient compared with networks with higher complexity. There are many pieces of research choosing AlexNet, which out-performed their state-of-the-art, e.g., Szymak and Gasiorowski [16] used pre-trained AlexNet for underwater object recognition. Guo *et al.* [17] employed the AlexNet model for inversion of PM2.5 atmospheric refractivity profile. Zhao *et al.* [18] utilized the AlexNet model to detect surface defects of wind turbine blades. Xiao *et al.* [19] proposed an improved AlexNet model that achieved a higher accuracy than the ZFNet model on a 23 categories classification task. The success of all these methods showed that AlexNet is excellent in feature extraction.

The integration of convolution into neural networks is well suited to the image classification, as a strong assumption of local spatial coherence can be made on images. As convolutional filters replace the dense connections within the multi-layered perceptron, the number of connections and trainable parameters can also be significantly reduced. Apart from the CNN structure, characteristics of the AlexNet also include local response normalization (LRN), rectified linear unit (ReLU), and dropout regularization [15].

Before the development of AlexNet, the standard activation function (AF) is either sigmoid

$$f(\zeta) = (1 + \mathrm{e}^{-\zeta})^{-1},$$

or hyperbolic tangent

$$f(\zeta) = \tanh(\zeta).$$

These functions suffer from saturation, where outputs are limited by the asymptotic bounds. Saturation restricts gradient flow during backpropagation and limits the overall capacity of the neural network [20]. The ReLU activation function used in AlexNet

$$f(\zeta) = \max(\zeta, 0),$$

has no upper bound and is therefore non-saturating.

Local response normalization (LPN) [15] is a technique used in AlexNet to normalize the unbounded ReLU activations and promote lateral inhibition, which enhances local contrasts and aids generalization. One core challenge in the training of neural networks is overfitting, which occurs when the irrelevant fluctuations in the training data are also captured by the neural network, resulting in lower generalization. Dropout reduces overfitting by freezing neurons in the neural network based on a set probability, equivalent to the generation of new neural networks during the training process. Dropout can effectively limit the co-adaptation of the neurons, and therefore reduce overfitting.

The AlexNet structure, shown in Fig.2(a), is highly versatile and often used in medical imaging, especially medical image classification. Gertych *et al.* [21] successfully applied ImageNet pre-trained AlexNet to distinguish lung cancer growth patterns in histological slides. To aid the diagnosis of rheumatoid arthritis, Fukae *et al.* [22] employed the same neural network in the classification of virtual images generated from clinical information.

We propose the use of a variant of the single GPU AlexNet structure (Net-0) as the backbone of our approach, due to the ease of implementation. As exhibited in Fig.2(b), we retain the general structure of AlexNet: five convolutional layers and multiple fully connected layers (FCLs). In the original AlexNet, there are three FCLs in total: FCL1, FCL2 and FCL3. We replace the last 1 000-neuron layer (FCL3) of the original AlexNet with an FCL with 512 neurons (FCL3*) and add an extra FCL with two neurons (FCL4*) to the top FCL3*, due to two reasons: 1) the universal approximation theorem [23]; 2) the fact that two neurons correspond to the two categories of our classification task. This AlexNet variant is called "Net-0".

4.2 Improvements

In order to further improve the backbone AlexNet proposed in Subsection 4.1, we incorporate batch normalization into the neural network structure. Batch normalization (BN) reduces the internal covariance shift within neural networks and promotes independence between layers. This effect is achieved by scaling each mini-batch of previous layer outputs with the mean and variance of that particular mini-batch. The process of this scaling adds noises to the mini-batches and, therefore, also provides regularization. AlexNet with BN can be trained with higher learning rates as BN provides bounds to the activation values. As seen in Fig.2(c), batch normalization is added to each convolutional layer. This modified structure is named Net-1.

We first train Net-1 on the training images to fine-tune the weights for better feature extraction in this classification task. The trained network is named Net-2.

4.3 Proposed Algorithm 1: DC-Net-S

AlexNet has been successfully applied in many fields. However, AlexNet requires a large dataset for

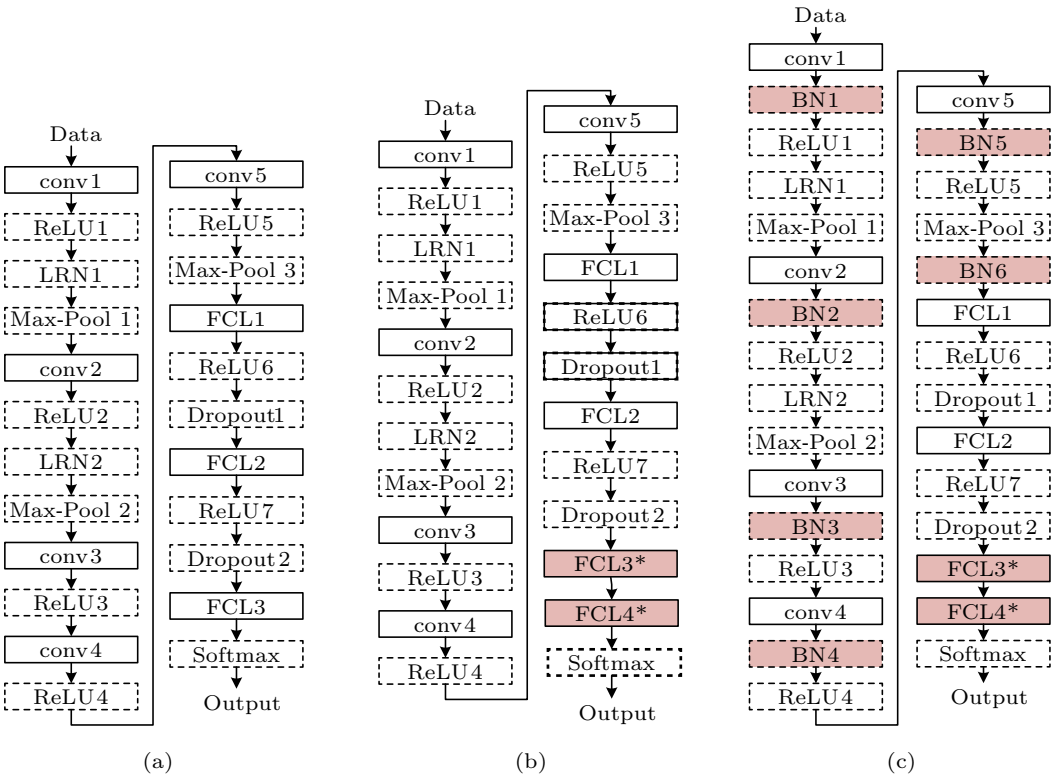

Fig.2. Structure comparison of (a) original, (b) adapted AlexNet, i.e., last FCL replaced (Net-0), and (c) BN added (Net-1). Solid boxes mean layers with learnable weights while no learnable weights are introduced in dotted boxes.

training to obtain good performance. As it is challenging for us to build a large dataset, we propose to use AlexNet as a pre-trained model for feature extraction only. Then, we employ three different randomized neural network classifiers attached to the trained AlexNet, including 1) extreme learning machine (ELM) [24]; 2) Schmidt neural network (SNN) [25]; 3) random vector functional-link net (RVFL) [26]. These deep COVID networks are abbreviated as DC-Nets.

We compare these three models and select the best. The three classifiers are selected because they can provide a good solution without iterations, and thus save computation time.

The first proposed model is DC-Net-S, in which the Schmidt neural network (SNN) [25] is used to replace the last three layers in Net-2. Let the i-th input sample $\boldsymbol{x}_i$ be $\boldsymbol{x}_i = (x_{i_1}, \cdots, x_{i_n})^{\mathrm{T}} \in \mathbb{R}^n, i = 1, \cdots, N$.

Let $\boldsymbol{y}_i = (y_{i_1}, y_{i_2}, \cdots, y_{i_m})^{\mathrm{T}} \in \mathbb{R}^m$ mean the i-th output information, and the structure of SNN is shown in Fig.3(a). For the SNN, we have $\hat{N}$ hidden nodes. The model can be expressed as:

$$\sum_{j=1}^{\hat{N}} \left(\boldsymbol{\lambda_j} g\left(\boldsymbol{\alpha}_j \boldsymbol{x}_i + \beta_j\right)\right) + \boldsymbol{\gamma} = \boldsymbol{O}_i, i = 1, \cdots, N,$$

in which $g(\cdot)$ is the sigmoid function. $\boldsymbol{\alpha}_j$ and β_j are randomly initialized and kept the same during training. $\boldsymbol{\gamma} = (\gamma_1, \gamma_2, \gamma_3, \cdots, \gamma_m)^{\mathrm{T}}$ denotes the output biases. $\boldsymbol{\lambda}_j$ can be calculated by pseudo-inverse. $\boldsymbol{O}_i = (o_{i1}, o_{i2}, o_{i3}, \cdots o_{im})^{\mathrm{T}}$ is the output of the model for the i-th sample.

4.4 Proposed Algorithm 2: DC-Net-E

We propose the second model: DC-Net-E, by substituting the last three layers in Net-2 with the ELM layers. ELMs are feedforward neural networks for regression, clustering, and classification and feature learning with a single layer [27]. Compared with the backpropagation-based networks, ELM excels in generalization performance as the parameters are more likely to achieve a better global best solution and less computation time as it does not depend on the gradient descent. The parameters of the hidden nodes do not need to be tuned. The structure of ELM is shown in Fig.3(b).

Given the training set as defined in Subsection 4.3, the mapping function of ELM can be expressed as

$$\sum_{j=1}^{\hat{N}} \boldsymbol{\lambda}_j g\left(\boldsymbol{\alpha}_j \boldsymbol{x}_i + \beta_j\right) = \boldsymbol{O}_i, \quad i = 1, \cdots, N,$$

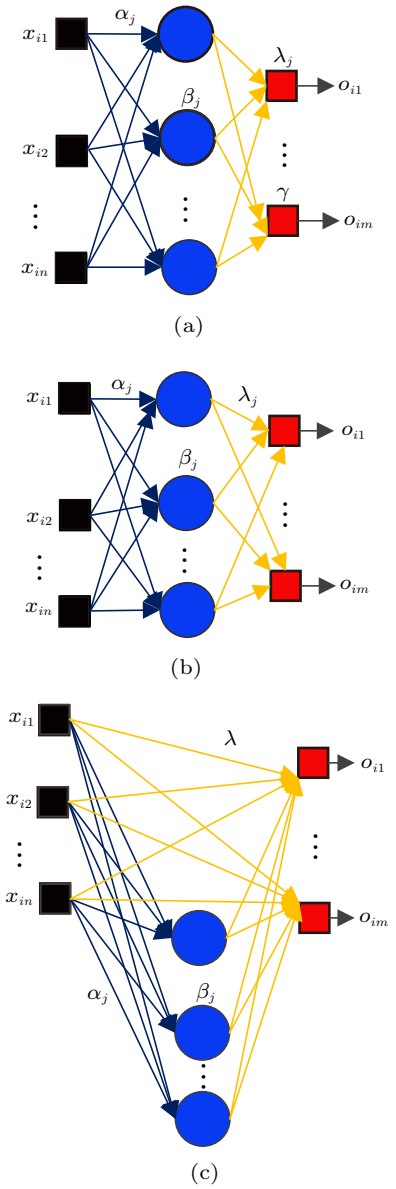

Fig.3. Structure of three randomized neural networks. (a) SNN. (b) ELM. (c) RVFL. (The black square boxes denote the input, and the circles filled in blue are hidden neurons in the hidden layer while the red square boxes are the output.)

where $\hat{N}$ means the number of hidden neurons. $\boldsymbol{\alpha}_i = (\alpha_{i_1}\alpha_{i_2}, \cdots, \alpha_{i_n})^{\mathrm{T}}$ stands for the input weight, and β_i denotes the bias. $\boldsymbol{O}_i = (o_{i1}, o_{i2}, o_{i3}, \cdots, o_{im})^{\mathrm{T}}$ is the output of the model for the i-th sample. This model is trained to achieve that

$$\sum_{j=1}^{\hat{N}} \boldsymbol{\lambda}_j g\left(\boldsymbol{\alpha}_j \boldsymbol{x}_i + \beta_j\right) = \boldsymbol{y}_i, \quad i = 1, \cdots, N.$$

We rewrite the equation as

$$\boldsymbol{M}\lambda = \boldsymbol{Y},$$

where

$$\boldsymbol{M}\left(\boldsymbol{\alpha}_1,\cdots,\boldsymbol{\alpha}_{\hat{N}},\beta_1,\cdots,\beta_{\hat{N}},\boldsymbol{x}_1,\cdots,\boldsymbol{x}_N\right) = \begin{pmatrix} g\left(\boldsymbol{\alpha}_1\boldsymbol{x}_1+\beta_1\right) & \cdots & g\left(\boldsymbol{\alpha}_{\hat{N}}\boldsymbol{x}_1+\beta_{\hat{N}}\right) \\ \vdots & \ddots & \vdots \\ g\left(\boldsymbol{\alpha}_1\boldsymbol{x}_N+\beta_1\right) & \cdots & g\left(\boldsymbol{\alpha}_{\hat{N}}\boldsymbol{x}_N+\beta_{\hat{N}}\right) \end{pmatrix}_{N\times\hat{N}}, \quad (1)$$

$$\boldsymbol{\lambda} = \begin{pmatrix} \boldsymbol{\lambda}_1^{\mathrm{T}} \\ \vdots \\ \boldsymbol{\lambda}_{\hat{N}}^{\mathrm{T}} \end{pmatrix}_{\hat{N}\times m}, \quad \boldsymbol{Y} = \begin{pmatrix} \boldsymbol{y}_1^{\mathrm{T}} \\ \vdots \\ \boldsymbol{y}_N^{\mathrm{T}} \end{pmatrix}_{N\times m}.$$

It has been proved that any single hidden layer network can asymptotically approximate the training samples based on the universal approximation theorem [28]. However, it is a big challenge to find the optimal $\boldsymbol{\alpha}_j$, β_j and $\boldsymbol{\lambda}_j$. ELM is one method that can provide a solution for the above model. The pseudocode is explained in Algorithm 1.

Algorithm 1. ELM

Input: $(\boldsymbol{x}_i, \boldsymbol{y}_i)$

Step 1: randomly initialize values of input weight $\boldsymbol{\alpha}_j$ and bias β_j

Step 2: calculate output matrix $\boldsymbol{M}$ using (1)

Step 3: compute output weight $\boldsymbol{\lambda}$ by pseudo inverse in (2)

Output: the trained ELM structure

Pseudo inverse:

$$\boldsymbol{\lambda} = \boldsymbol{M}^{\dagger}\boldsymbol{Y}, \quad (2)$$

in which $\boldsymbol{M}^{\dagger}$ represents the Moore-Penrose of $\boldsymbol{M}$.

4.5 Proposed Algorithm 3: DC-Net-R

The third proposed model is named DC-Net-R. For this model, the last three layers in Net-2 are replaced with RVFL layers [26], whose structure is shown in Fig.3(c).

Different from traditional Single-Layer Feedforward Neural-network (SLFN) that successively maps its inputs to the outputs until the known mapping achieves the required accuracy, RVFL first maps the input to the enhancement nodes as expressed in (3), and then the feature vector is formed by concatenating the two spaces [29]. Finally, the output nodes and the concatenated feature space are linked by another mapping function. $\boldsymbol{\alpha}_j$, β_j and $\boldsymbol{\lambda}$ stand for weights, bias and output weight respectively. In Fig.3(c), the input weights are in blue and the output layer weights are in yellow.

For the enhancement layer, we have an AF. Then, input weights and bias values are both randomly assigned values, and the output weights could be attained via pseudo-inverse.

$$\boldsymbol{V} = \sum_{j=1}^{\hat{N}} g(\boldsymbol{a}_j\boldsymbol{x}+\beta_j), \quad (3)$$

where $\boldsymbol{x} = (\boldsymbol{x}_1,\cdots,\boldsymbol{x}_N)^{\mathrm{T}}$. The loss function of RVFL is expressed as

$$E = \frac{1}{2N}\sum_{n=1}^{N}\left(\boldsymbol{y}^{(\boldsymbol{n})} - \boldsymbol{\lambda}\mathbb{W}^{(n)}\right)^2,$$

where $\boldsymbol{\lambda}$ means the output weight values. $\boldsymbol{V}$ is the enhanced pattern vector, and n is the pattern index. $\mathbb{W}$ is the concatenation of $\boldsymbol{x}$ and $\boldsymbol{V}$.

$$\mathbb{W} = \mathrm{concat}(\boldsymbol{x}, \boldsymbol{V}).$$

4.6 Implementation

Algorithm 2 shows the pseudocode of the proposed three DC-Net models, and Fig.4 provides the flowchart of the proposed three DC-Net models.

Algorithm 2. Applying Proposed DC-Net Models to Detect COVID-19

Input: the training set and test set

Step 1: AlexNet pre-trained on ImageNet is loaded;

Step 2: Remove last FCL, add two new FCLs, and we get "Net-0";

Step 3: Based on Net-0, we add BN Layers, and get "Net-1";

Step 4: Fine-tuning Net-1 with COVID training set, output "Net-2";

Step 5: Generate training features via NET-2 from training images;

Step 6: For $k = 1:10$

- Step 6.1: Set the seed randomly;
- Step 6.2: Train SNN, ELM, and RVFL using training features and training labels;
- Step 6.3: Combine Net-2 and trained SNN, ELM, and RVFL;
- Step 6.4: Create three DC-Nets: DC-Net-S, DC-Net-E, and DC-Net-R;
- Step 6.5: Input test images to three proposed models;
- Step 6.6: Generate the performance at the k-th run by the predicted labels and the actual test labels;

End

Step 7: Output the average performances of three proposed DC-Net models;

Step 8: Select the optimal DC-Net model in terms of classification performances.

Output: the optimal DC-Net model and its classification statistics

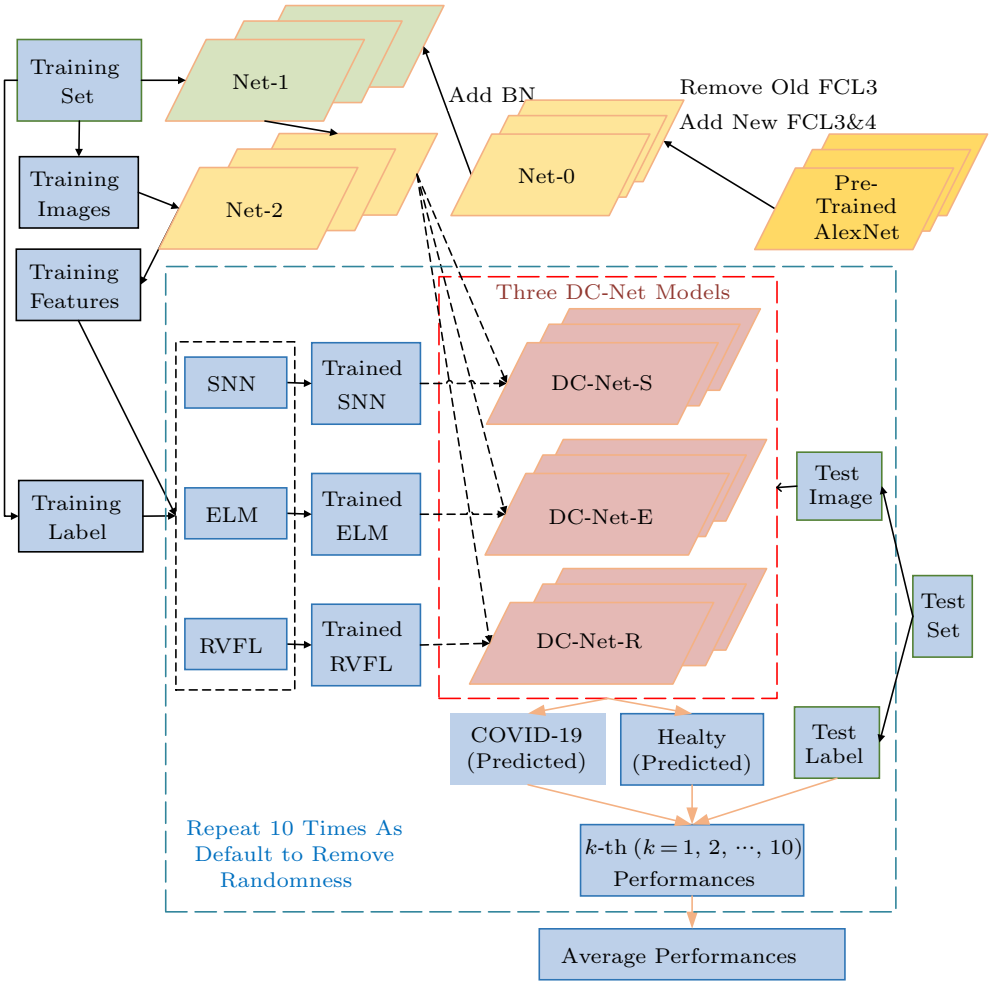

Fig.4. Flowchart of applying the three DC-Net models to detect COVID-19.

The first step is to input the training set and the test set and generate features via Net-1 and Net-2. Note that original images in the dataset are RGB images with the size of 512×512 pixels. Therefore, they are resized to 227×227 pixels to meet the input requirement of AlexNet. Then, extracted features are fed into the three classifiers for training until stopping criteria are met. Then we select the classifier with the best performance. We finally get the trained DC-Net and predicted labels. The performance is evaluated by comparing the predicted labels with the ground truth labels.

5 Experiment Settings

The training parameters are shown in Table 2. We set the MiniBatchSize as 20, MaxEpochs as 20 and InitialLearnRate as 10^{-4}. We select stochastic gradient descent with momentum (SGDM) [30] to be the training algorithm. All above hyperparameters are selected by the trial-and-error method.

Table 2. Training Parameters

Parameter	Value
Training algorithm	SGDM
MiniBatchSize	20
MaxEpochs	20
InitialLearnRate	10^{-4}

To assess the performance of the three proposed DC-Nets, we split the dataset: 70% of the samples are included in the training set, and the other 30% are the testing set. The reason why we use hold-out validation is that our model can be better evaluated using hold-out validation than using cross-validation because the number of images is relatively small. Numerous studies are also evaluated based on the hold-out testing set due to the small size of the dataset [31].

The AlexNet variant in Subsection 4.2 is first

trained with the training set and parameters shown in Table 2. Using Net-2, we can extract the input to the final FCL layer, i.e., activations of FCL3, for each sample. These activations represent the extracted features from the baseline model and are used as input for the proposed algorithms. Each algorithm is trained with the training features and then evaluated on the test set. This process of the hold-out validation is repeated 10 times, where each run initializes with a new set of random weights. The average of 10 runs is the final result. This process can effectively limit the effect of individual stochastic weight initialization on performance. The reason why we set the number of runs to 10 is that it is a default setting in many other machine learning studies.

In each evaluation, the predictions of all the three DC-Nets are compared with the ground truth. We denote the number of patients accurately classified as TP and misclassified as FN, and the number of healthy controls accurately classified as TN and misclassified as FP. The metrics used to evaluate performance include:

1) sensitivity: the percentage of patients accurately classified

$$Sensitivity = \frac{TP}{TP + FN},$$

2) specificity: the percentage of healthy controls accurately classified

$$Specificity = \frac{TN}{TN + FP},$$

3) precision: the percentage of predicted patients that are actual patients

$$Precision = \frac{TP}{TP + FP},$$

4) accuracy: the percentage of correct classification

$$Accuracy = \frac{TP + TN}{TP + FP + TN + FN},$$

5) $F1$ score: the measure of classification ability

$$F1 = 2 \times \frac{Precision \times Sensitivity}{Precision + Sensitivity}.$$

6 Results and Discussion

6.1 Effect of BN

In order to justify the integration of batch normalization into AlexNet, we train and evaluate both Net-0 and Net-1. The iteration-wise plot of training accuracy and losses of Net-0 and Net-1 are shown in Figs.5(a) and 5(b) respectively. At the same learning rate, we can observe that the loss of Net-1 is significantly lower than that of Net-0 in the first few iterations.

Net-1 also shows a lower variation in the decline of loss than Net-0, indicating faster convergence and higher stability. This effect is consistent with BN's characteristic described in Subsection 4.2 and is further validated by the test results shown in Table 3.

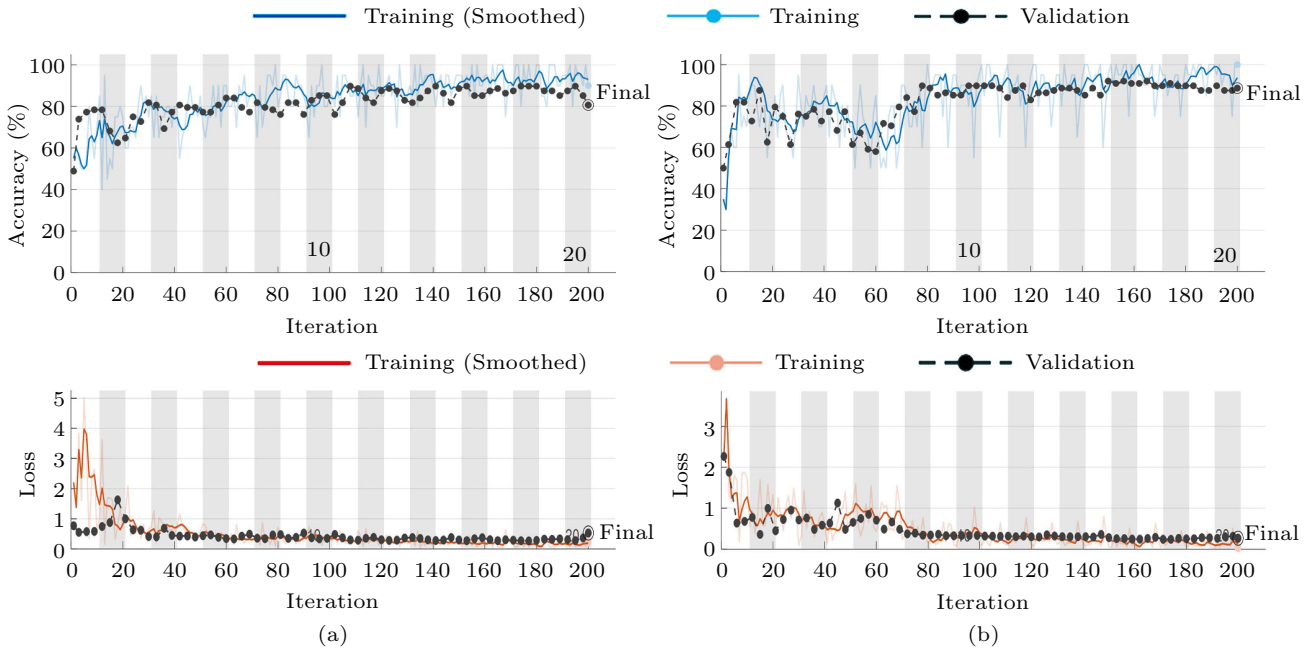

Fig.5. Convergence plot. (a) Net-0. (b) Net-1.

Table 3. Comparison of Net-0 and Net-1

Measure	CM	Accuracy
Net-0	$\begin{pmatrix} 30 & 14 \\ 3 & 41 \end{pmatrix}$	0.806 8
Net-1	$\begin{pmatrix} 39 & 5 \\ 4 & 40 \end{pmatrix}$	0.880 0

Note: CM: Confusion Matrix.

6.2 Comparison Among Three DC-Net Models

We can see from Table 4 the mean accuracy of DC-Net-R is 90.91%. Comparative results of DC-Net-E and DC-Net-S show their mean accuracies are 90.34% and 90.23% respectively. DC-Net-R shows the best precision and specificity amongst these algorithms in testing. A possible explanation for the result is the existence of a direct connection between input and output in DC-Net-R, as shown in Fig. 3(c). A possible explanation for DC-Net-E to show a higher testing accuracy than DC-Net-S is the higher number of trainable parameters. DC-Net-E has a bias for each corresponding weight. In contrast, DC-Net-S only has a single bias value for all weights.

6.3 Comparison with Other Methods

To validate the efficacy of our DC-Net models, we also compare our methods (i.e., previous models) with seven other methods. With no specification, we use the aforementioned parameters in Table 2 when training all of the models. To provide a fair comparison, we adapt all referred methods correspondingly to the classification task here. CTIs are resized to meet the input requirements of different networks. The comparison results are given in Table 5.

Our proposed DC-Nets show the best performance in every aspect compared with other methods, especially when compared with the hand-crafted features based methods [3–5]. There are two main reasons why our methods perform best. One is that activation layers extract more representative high-level features in Net-2. The other is the structural superiority of RVFL that allows resilient updates of parameters.

For each method in Table 5, images are adjusted accordingly to meet the input requirements. For Net-2-RF (Random Forest) and Net-2-SVM (Support Vector Machine), both features are extracted from Net-2 through FCL3 while there are five decision trees in the forest. SVM gives identical results during each running

Table 4. Test Performance Comparison of Three Classifiers: DC-Net-E, DC-Net-S, and DC-Net-R

Algorithm	Sensitivity	Specificity	Precision	Accuracy	$F1$
DC-Net-E	**0.8864 ± 0.0240**	0.920 4 ± 0.045 8	0.920 0 ± 0.043 8	0.903 4 ± 0.019 5	0.902 0 ± 0.018 2
DC-Net-S	0.881 8 ± 0.025 8	0.922 7 ± 0.035 8	0.920 7 ± 0.034 7	0.902 3 ± 0.020 2	0.900 4 ± 0.020 1
DC-Net-R	0.856 8 ± 0.015 3	**0.961 3 ± 0.011 0**	**0.957 0 ± 0.011 9**	**0.909 1 ± 0.009 3**	**0.904 1 ± 0.010 1**

Note: The best performance is in bold.

Table 5. Comparison of Proposed Methods with Other Methods

Method	Sensitivity	Specificity	Precision	Accuracy	$F1$
RBFNN [3]	0.659 1	0.750 0	0.725 0	0.704 5	0.690 5
K-ELM [4]	0.568 2	0.613 6	0.595 2	0.590 9	0.581 4
ELM-BA [5]	0.550 0 ± 0.025 8	0.763 6 ± 0.024 4	0.699 7 ± 0.024 4	0.656 8 ± 0.019 2	0.615 6 ± 0.022 5
RCBBO [6]	0.763 6 ± 0.046 8	0.777 3 ± 0.036 4	0.774 9 ± 0.031 9	0.770 5 ± 0.030 8	0.768 5 ± 0.033 5
6L-CNN [7]	0.831 8 ± 0.023 2	0.829 5 ± 0.023 3	0.830 7 ± 0.017 2	0.830 7 ± 0.010 7	0.830 8 ± 0.011 3
GoogLeNet [8]	0.775 0 ± 0.037 8	0.843 2 ± 0.065 6	0.836 5 ± 0.052 5	0.809 1 ± 0.021 3	0.802 6 ± 0.016 5
ResNet18 [9]	0.750 0 ± 0.056 7	0.936 4 ± 0.027 9	0.923 8 ± 0.029 5	0.843 2 ± 0.022 0	0.826 1 ± 0.030 9
Net-2-RF	0.881 8 ± 0.031 8	0.870 5 ± 0.066 1	0.875 6 ± 0.057 7	0.876 1 ± 0.033 2	0.877 4 ± 0.030 4
Net-2-SVM	0.909 1	0.840 9	0.851 1	0.875 0	0.879 1
DC-Net-E	**0.8864 ± 0.0240**	0.920 4 ± 0.0458	0.920 0 ± 0.0438	0.903 4 ± 0.0195	0.902 0 ± 0.0182
DC-Net-S	0.881 8 ± 0.025 8	0.922 7 ± 0.035 8	0.920 7 ± 0.034 7	0.902 3 ± 0.020 2	0.900 4 ± 0.020 1
DC-Net-R (Ours)	0.856 8 ± 0.015 3	**0.961 3 ± 0.011 0**	**0.957 0 ± 0.011 9**	**0.909 1 ± 0.009 3**	**0.904 1 ± 0.010 1**

Note: The best performance is in bold.

so that there is no variation of results. From the viewpoint of radiologists, spiral CCT is still a reliable and rapid technique for diagnosing and screening COVID-19. Nevertheless, due to a large number of patients and the need for multiple reviews in a short time, the huge number of CTIs significantly increases the workload of the radiologists. Furthermore, different radiologists have various skill levels and may be affected by subjective factors and external pressure. Misdiagnosis and missed diagnosis may delay diagnosis and patient isolation, which facilitates the spread of disease, and eventually alters the overall control of the COVID-19 epidemic. Therefore, there is an urgent need to develop a precise computer-aided method to assist clinicians in identifying patients with COVID-19 infection from CTIs.

DL is a critical innovation in the arena of artificial intelligence (AI). It has achieved excellent results in the field of radiology. Existing researches have efficaciously applied DL approaches to detect pneumonia in pediatric chest X-rays (PCXRs). They further distinguished viral pneumonia from bacterial pneumonia using two-dimensional PCXRs [32]. On low-dose CCT, Ardila *et al.* [33] accomplished an end-to-end model to detect lung cancer. The AUC of their method achieves almost 95%. Chae *et al.* [34] employed CNNs to classify trivial objects ($\leqslant 2$ cm) as lung nodules within CT scan images. However, there are few reports on COVID-19 in deep learning. We use DL to detect CTIs of COVID-19 pneumonia in this research.

Typical CT of COVID-19 patients shows sub-pleural GG-like patterns, which can 1) affect both lungs and 2) be multiple and peripheral and diffusely distributed. According to the imaging mode, there are many characteristics that can identify viral pathogens. These features are related to their specific pathogenesis [35], which prove that the deep learning method can be used to extract the image features for COVID-19 diagnosis. The GG in CTI may be one of the most key characteristics for identifying lesions. For that reason, we apply the deep learning model in the GG sample in the CTIs. We develop a DL-based lung CT diagnostic framework DC-Net to diagnose COVID-19 cases. The system can automatically extract GG samples of COVID-19 new pneumonia from image pictures and other radiological characteristics.

We invent and evaluate the DL framework used for detection from the CTIs of the chests of COVID-19 patients. The study gathers 66 COVID-19 confirmed patients from the Huai'an Infectious Disease Hospital in China and 66 healthy patients. As a result of the CT scan of the human chest, we collect 148 CTIs of confirmed COVID-19 cases and CITs of normal people for comparison and modelling. This is a retrospective, multi-cohort, diagnostic study. Our results show that the model has high sensitivity (0.856 8), high specificity (0.961 3), high precision (0.957 0), and high accuracy (0.909 1). Due to the powerful function of detail extraction, the performance of RVFL is better than that of ELM and SNN. The high performance of those DL models shows that the CTIs of both COVID-19 cases and normal subjects can be satisfactorily distinguished. The results show that the use of deep learning methods to extract imaging graphics features is of vast value for the diagnosis of COVID-19.

6.4 Time Analysis

The time comparison of manual diagnosis and our DC-Net models is presented in Table 6. It can be observed that a senior radiologist requires 76.590 9 seconds to make a diagnosis on average, which is appropriately half of the time for the junior radiologist of 142.590 9 seconds.

Table 6. Time Comparison of Image Interpreting (s)

Image	JR	SR	DC-Net-E	DC-Net-S	DC-Net-R
1	150.000 0	52.000 0	0.006 3	0.005 1	0.005 4
2	140.000 0	57.000 0	0.006 0	0.004 7	0.005 3
3	130.000 0	52.000 0	0.005 4	0.005 3	0.004 9
4	142.000 0	70.000 0	0.005 1	0.005 5	0.005 1
5	169.000 0	64.000 0	0.006 4	0.004 9	0.005 4
6	140.000 0	70.000 0	0.005 8	0.005 0	0.004 9
7	150.000 0	68.000 0	0.006 0	0.006 2	0.005 1
8	145.000 0	80.000 0	0.006 5	0.005 5	0.005 6
9	170.000 0	60.000 0	0.005 5	0.005 2	0.005 1
10	140.000 0	82.000 0	0.005 7	0.004 8	0.005 3
11	150.000 0	72.000 0	0.005 3	0.005 1	0.005 0
12	146.000 0	67.000 0	0.005 2	0.004 8	0.005 3
13	129.000 0	94.000 0	0.005 2	0.005 5	0.005 5
14	139.000 0	89.000 0	0.0054	0.0049	0.0058
15	148.000 0	69.000 0	0.005 3	0.005 0	0.005 1
16	130.000 0	102.000 0	0.005 3	0.004 8	0.005 5
17	129.000 0	84.000 0	0.005 4	0.005 8	0.005 2
18	136.000 0	95.000 0	0.005 5	0.004 6	0.005 1
19	142.000 0	88.000 0	0.005 7	0.005 3	0.005 3
20	139.000 0	101.000 0	0.005 2	0.004 7	0.005 5
21	130.000 0	85.000 0	0.005 0	0.004 8	0.004 9
22	143.000 0	84.000 0	0.004 9	0.004 8	0.005 0
Mean	142.590 9	76.590 9	0.005 6	0.005 1	0.005 2

Note: JR: junior radiologist; SR: senior radiologist.

However, our three DC-Nets can deliver the diagnosis result within about half of a millisecond, which is over 10 000 times faster than a senior radiologist. Therefore, the proposed models can be used in real-world situations without long-time endurance.

7 Conclusions

In this study, we proposed three DC-Net models (DC-Net-S, DC-Net-E, and DC-Net-R) for the classification of new coronavirus pneumonia in CTIs. The DC-Net-R structure uses batch normalization incorporated AlexNet variant with the RVFL algorithm. The comparative study among DC-Net-S, DC-Net-E, and DC-Net-R shows the last DC-Net-R as a viable and potential choice for neural networks in this classification task.

Our research proved that the deep learning method can automatically identify lesions from CTIs and detect COVID-19 patients effectively for doctors. Artificial intelligence can be used as a preliminary screening tool to reduce the pressure on front-line radiologists and reduced misdiagnosis rate of COVID-19 patients. AI can also accelerate the diagnosis of radiation and has great potential to recuperate early diagnosis, treatment, and isolation, thereby helping to contain epidemics.

This study has one limitation. The training dataset is relatively small and is collected from a single hospital, thereby it cannot form a representative distribution for the general population. In the future we shall collect more CT examinations from other hospitals to evaluate the detection efficiency of our model.

Acknowledgement We thank Qinghua Zhou from University of Leicester who helped in paper-writing and English checking.

References

[1] Wang C, Horby P W, Hayden F G, Gao G F. A novel coronavirus outbreak of global health concern. *The Lancet*, 2020, 395(10223): 470-473. DOI: 10.1016/S0140-6736(20)30185-9.

[2] Wang D, Hu B, Hu C *et al.* Clinical characteristics of 138 hospitalized patients with 2019 novel coronavirus-infected pneumonia in Wuhan, China. *JAMA*, 2020, 323(11): 1061-1069. DOI: 10.1001/jama.2020.1585.

[3] Lu Z, Lu S Y, Liu G *et al.* A pathological brain detection system based on radial basis function neural network. *Journal of Medical Imaging and Health Informatics*, 2016, 6(5): 1218-1222. DOI: 10.1166/jmihi.2016.1901.

[4] Yang J, Qiu X, Shi J P *et al.* A pathological brain detection system based on kernel based ELM. *Multimedia Tools and Applications*, 2018, 77(3): 3715-3728. DOI: 10.1007/s11042-016-3559-z.

[5] Lu S, Qiu X, Shi J P *et al.* A pathological brain detection system based on extreme learning machine optimized by bat algorithm. *CNS & Neurological Disorders-Drug Targets*, 2017, 16(1): 23-29. DOI: 10.2174/1871527315666161019153259.

[6] Wang S H, Li P, Chen P *et al.* Pathological brain detection via wavelet packet Tsallis entropy and real-coded biogeography-based optimization. *Fundamenta Informaticae*, 2017, 151(1/2/3/4): 275-291. DOI: 10.3233/FI-2017-1492.

[7] Jiang X, Zhang Y. Chinese sign language fingerspelling recognition via six-layer convolutional neural network with leaky rectified linear units for therapy and rehabilitation. *Journal of Medical Imaging and Health Informatics*, 2019, 9(9): 2031-2038. DOI: 10.1166/jmihi.2019.2804.

[8] Szegedy C, Liu W, Jia Y *et al.* Going deeper with convolutions. In *Proc. the 2015 IEEE Conference on Computer Vision and Pattern Recognition*, June 2015, pp.1-9. DOI: 10.1109/CVPR.2015.7298594.

[9] Yu X, Wang S H. Abnormality diagnosis in mammograms by transfer learning based on ResNet18. *Fundamenta Informaticae*, 2019, 168(2/3/4): 219-230. DOI: 10.3233/FI-2019-1829.

[10] Peng H, Long F, Ding C. Feature selection based on mutual information criteria of max-dependency, max-relevance, and min-redundancy. *IEEE Transactions on Pattern Analysis and Machine Intelligence*, 2005, 27(8): 1226-1238. DOI: 10.1109/TPAMI.2005.159.

[11] Chung M, Bernheim A, Mei X *et al.* CT imaging features of 2019 novel coronavirus (2019-nCoV). *Radiology*, 2020, 295(1): 202-207. DOI: 10.1148/radiol.2020200230.

[12] Maghdid H S, Ghafoor K Z, Sadiq A S *et al.* A novel AI-enabled framework to diagnose coronavirus COVID 19 using smartphone embedded sensors: Design study. arXiv:2003.07434, 2020. https://arxiv.org/abs/2003.07434, Dec. 2020.

[13] Wang L, Wong A. COVID-Net: A tailored deep convolutional neural network design for detection of COVID-19 cases from chest radiography images. arXiv:2003.09871, 2020. https://arxiv.org/abs/2003.09871, Dec. 2020.

[14] Al-Karawi D, Al-Zaidi S, Polus N, Jassim S. Machine learning analysis of chest CT scan images as a complementary digital test of coronavirus (COVID-19) patients. *medRxiv*. DOI: 10.1101/2020.04.13.20063479.

[15] Krizhevsky A, Sutskever I, Hinton G E. ImageNet classification with deep convolutional neural networks. In *Proc. the 25th International Conference on Neural Information Processing Systems*, December 2012, pp.1097-1105. DOI: 10.1145/3065386.

[16] Szymak P, Gasiorowski M. Using pretrained AlexNet deep learning neural network for recognition of underwater objects. *Naše More*, 2020, 67(1): 9-13. DOI: 10.17818/NM/2020/1.2.

[17] Guo C J, Xu Y L, Tian Z. Inversion of PM2.5 atmospheric refractivity profile based on AlexNet model from the perspective of electromagnetic wave propagation. *Environmental Science and Pollution Research*, 2020, 27(30): 37333-37346. DOI: 10.1007/s11356-020-07703-w.

[18] Zhao X Y, Dong C Y, Zhou P, Zhu M J, Ren J W, Chen X Y. Detecting surface defects of wind tubine blades using an Alexnet deep learning algorithm. *IEICE Transactions on Fundamentals of Electronics Communications and Computer Sciences*, 2019, E102A(12): 1817-1824. DOI: 10.1587/transfun.E102.A.1817.

[19] Xiao L, Yan Q, Deng S. Scene classification with improved AlexNet model. In *Proc. the 12th International Conference on Intelligent Systems and Knowledge Engineering*, Nov. 2017. DOI: 10.1109/ISKE.2017.8258820.

[20] Rakitianskaia A, Engelbrecht A. Measuring saturation in neural networks. In *Proc. the 2015 IEEE Symposium Series on Computational Intelligence*, Dec. 2015, pp.1423-1430. DOI: 10.1109/SSCI.2015.202.

[21] Gertych A, Swiderska-Chadaj Z, Ma Z *et al.* Convolutional neural networks can accurately distinguish four histologic growth patterns of lung adenocarcinoma in digital slides. *Sci. Rep.,* 2019, 9(1): Article No. 1483. DOI: 10.1038/s41598-018-37638-9.

[22] Fukae J, Isobe M, Hattori T *et al.* Convolutional neural network for classification of two-dimensional array images generated from clinical information may support diagnosis of rheumatoid arthritis. *Sci. Rep.*, 2020, 10(1): Article No. 5648. DOI: 10.1038/s41598-020-62634-3.

[23] Nguyen H D, Lloyd-Jones L R, McLachlan G J. A universal approximation theorem for mixture-of-experts models. *Neural Computation*, 2016, 28(12): 2585-2593. DOI: 10.1162/NECO_a_00892.

[24] Huang Y, Yang D, Wang K, Wang L, Fan J. A quality diagnosis method of GMAW based on improved empirical mode decomposition and extreme learning machine. *Journal of Manufacturing Processes*, 2020, 54: 120-128. DOI: 10.1016/j.jmapro.2020.03.006.

[25] Schmidt W F, Kraaijveld M A, Duin R P W. Feedforward neural networks with random weights. In *Proc. the 11th IAPR International Conference on Pattern Recognition. Vol.II. Conference B: Pattern Recognition Methodology and Systems*, Aug. 30-Sept. 3, 1992. DOI: 10.1109/ICPR.1992.201708.

[26] Pao Y H, Park G H, Sobajic D J. Learning and generalization characteristics of the random vector functional-link net. *Neurocomputing,* 1994, 6(2): 163-180. DOI: 10.1016/0925-2312(94)90053-1.

[27] Kushwah G S, Ranga V. Voting extreme learning machine based distributed denial of service attack detection in cloud computing. *Journal of Information Security and Applications*, 2020, 53: Article No. 102532. DOI: 10.1016/j.jisa.2020.102532.

[28] Yager R R, Kreinovich V. Universal approximation theorem for uninorm-based fuzzy systems modeling. *Fuzzy Sets and Systems*, 2003, 140(2): 331-339. DOI: 10.1016/S0165-0114(02)00521-3.

[29] Scardapane S, Fierimonte R, Wang D H, Panella M, Uncini A. Distributed music classification using random vector functional-link nets. In *Proc. the 2015 International Joint Conference on Neural Networks*, July 2015. DOI: 10.1109/IJCNN.2015.7280333.

[30] Chaudhuri A. The minimization of empirical risk through stochastic gradient descent with momentum algorithms. In *Proc. the 8th Computer Science On-Line Conference on Artificial Intelligence Methods in Intelligent Algorithms*, April 2019, pp.168-181. DOI: 10.1007/978-3-030-19810-7_17.

[31] Dean J, Corrado G, Monga R *et al.* Large scale distributed deep networks. In *Proc. the 25th International Conference on Neural Information Processing Systems*, December 2012, pp.1223-1231.

[32] Rajaraman S, Candemir S, Kim I, Thoma G, Antani S. Visualization and interpretation of convolutional neural network predictions in detecting pneumonia in pediatric chest radiographs. *Applied Sciences*, 2018, 8(10): Article No. 1715. DOI: 10.3390/app8101715.

[33] Ardila D, Kiraly A P, Bharadwaj S *et al.* End-to-end lung cancer screening with three-dimensional deep learning on low-dose chest computed tomography. *Nature Medicine*, 2019, 25(6): 954-961. DOI: 10.1038/s41591-019-0447-x.

[34] Chae K J, Jin G Y, Ko S B, Wang Y, Zhang H, Choi E J, Choi H. Deep learning for the classification of small ($\leqslant$2 cm) pulmonary nodules on CT imaging: A preliminary study. *Acad. Radiol.*, 2020, 27(4): e55-e63. DOI: 10.1016/j.acra.2019.05.018.

[35] Koo H J, Lim S, Choe J, Choi S H, Sung H, Do K H. Radiographic and CT features of viral pneumonia. *RadioGraphics*, 2018, 38(3): 719-739. DOI: 10.1148/rg.2018170048.

Xin Zhang obtained his Bachelor's degree in medical imaging from Nanjing Medical University, Nanjing, in 2005, and his Master's degree in medical imaging from Qingdao University, Qingdao, in 2016. Professor Xin Zhang is currently the director of Department of Medical Imaging of The Fourth People's Hospital of Huai'an, Huai'an. His main research interests are imaging technology and diagnosis, and artificial intelligence.

Siyuan Lu received his B.S. and M.S. degrees in Nanjing Normal University, Nanjing, in 2014 and 2018, respectively. Now he is a Ph.D. candidate in University of Leicester, Leicester, majoring in image processing and machine learning.

Shui-Hua Wang received her B.S. degree from Southeast University, Nanjing (2005–2008), and her M.S. degree from The City University of New York, New York (2010–2012). She worked as a research assistant in Columbia University, New York (2012–2014). She received her Ph.D. degree from Nanjing University, Nanjing (2014–2017). She worked as a research associate in Loughborough University, Loughborough (2018–2019). She is now working as a research fellow in University of Leicester, Leicester. She received 2019 Web of Science Highly Cited Researcher Award.

Xiang Yu received his B.S. degree and Master's degree from Huanggang Normal University, Huanggang, and Xiamen University, Xiamen, in 2014 and 2018 respectively. Currently, he is a Ph.D. student and graduate teaching assistant (GTA) of University of Leicester, Leicester. His research interests include digital image segmentation, machine learning and deep learning.

Su-Jing Wang is an associate researcher and Master supervisor at Chinese Academy of Sciences, Beijing. He received his Ph.D. degree from Jilin University, Changchun, in 2012. He was a postdoctoral researcher at the Institute of Psychology, University of Chinese Academy of Sciences, Beijing, from 2012 to 2015. Since July 2015, he has joined the Chinese Academy of Sciences, Beijing. He was called as Chinese Hawking by the Xinhua News Agency.

Lun Yao is a vice president of The Fourth People's Hospital of Huai'an, Huai'an. He is a chief physician graduated from Nanjing Medical College, Nanjing. He has engaged in clinical gastroenterology and infectious diseases for more than 30 years.

Yi Pan received his B.Eng. and M.Eng. degrees in computer engineering from Tsinghua University, Beijing, in 1982 and 1984, respectively, and his Ph.D. degree in computer science from the University of Pittsburgh, Pittsburgh, in 1991. His profile has been featured as a distinguished alumnus in both Tsinghua Alumni Newsletter and University of Pittsburgh CS Alumni Newsletter. Dr. Pan's current research interests include bioinformatics, parallel and cloud computing, and big data. Dr. Pan has published more than 450 papers including over 250 journal papers and 100 IEEE/ACM Transactions/Journal papers. In addition, he has edited/authored 43 books. His work has been cited more than 14 000 times based on Google Scholar and his current h-index is 74.

Yu-Dong Zhang received his Ph.D. degree from Southeast University, Nanjing, in 2010. He worked as a postdoc from 2010 to 2012 with Columbia University, New York, and as an assistant research scientist from 2012 to 2013 with Research Foundation of Mental Hygiene (RFMH), New York. Now he serves as a professor with University of Leicester, Leicester, UK. Prof. Zhang was the 2019 & 2021 recipient of "Web of Science Highly Cited Researcher".